Analytic Model of Proprotor Forces and Moments at High Incidence

Yuchen Leng
Ph.D. candidate
ISAE-SUPAERO, ENAC, Delair
Toulouse, France

Thierry Jardin*
Research scientist

Jean-Marc Moschetta
Professor

DAEP, ISAE-SUPAERO, Toulouse, France

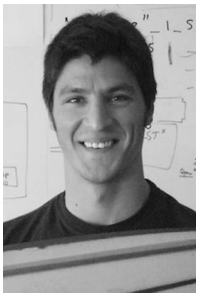

Murat Bronz
Associate Professor
UAV Lab, ENAC
Toulouse, France

The paper presents an analytical model for estimation of proprotor aerodynamic loads at elevated incidence angles. Previous theories have concentrated on either small incidence angle for aircraft stability analysis or edge-wise flow for helicopter forward flight. This development attempted an engineering method that covers the full incidence angle range from 0 to $\pi/2$. Blade element theory was applied to known proprotor geometry, and off-axis loads including normal force and in-plane moment were obtained in closed form based on thrust and torque in axial condition. The model was found to be sufficiently accurate over a broader flight conditions compared to classical models, and computationally more efficient than numerical methods. Hence it could be easily used as a preliminary design and analysis tool for future convertible aircraft proprotors. The paper further discusses a dedicated wind tunnel campaign on proprotor off-axis load measurement. Experimental data from the test campaign was considered in model validation. The results suggested that the model was capable to accurately estimate proprotor performance in nominal flight regimes.

Nomenclature

A	dynamic pressure correction factor, see Eq. (35)
B	inflow angle correction factor, see Eq. (36)
C_D	drag coefficient
C_L	lift coefficient
C_N	normal force coefficient
C_n	in-plane moment coefficient
C_Q	torque coefficient
C_T	thrust coefficient
D	proprotor diameter, m
f	slipstream dynamic pressure correction function
F_T	blade sectional tangential force, N/m
I_1, I_2, I_3	geometric integrals, Eqs. (29)–(31)
k_a	sidewash factor
k_s	spinner factor
L_x	vertical offset between proprotor and balance frame, m
L_z	longitudinal offset between proprotor and balance frame, m
m	geometric parameter, Eq. (33)
N	normal force, N
n	in-plane moment, Nm
p	pitch moment, Nm
Q	torque, Nm
R	blade radius, m
Re	Reynolds number
r	radius, m
S_p	proprotor disk area, $S_p = \pi R^2$, m^2
T	thrust, N
V_i	induced velocity, m/s
V_∞	freestream velocity, m/s
W	relative wind velocity, m/s
Y	side force, N

Greek symbols

α	airfoil angle of attack, rad
α_{ac}	aircraft angle of attack, rad
α_p	proprotor incidence angle, rad
β	blade pitch angle, rad
β_{ac}	aircraft side-slip angle, rad
Δ	geometry parameter, Eq. (32)
δ	edgewise flow correction factor, Eq. (23)
η_T, η_P	high incidence thrust and power correction factors, Eqs. (9) and (10)
λ_c	rotor climb inflow ratio, $V_\infty \sin\alpha_p / \Omega R$
λ_i	induced inflow ratio, $V_i / \Omega R$
λ_∞	proprotor tip speed ratio, $V_\infty / \Omega R$
$\lambda_{\infty_{0T}}$, $\lambda_{\infty_{0P}}$	zero-thrust and zero-power tip speed ratios
μ	rotor advance ratio, $V_\infty \cos\alpha_p / \Omega R$
ρ	air density, kg/m^3
σ	proprotor solidity
ϕ	inflow angle, rad
ψ	azimuth angle, rad
Ω	angular speed, rad/s

*Corresponding author; email: thierry.jardin@isae-supaero.fr

Manuscript received January 2020, accepted June 2021.

Attributes

$_0$	static structural load
$_A$	axial direction
$_b$	balance frame
$_p$	proprotor frame
$_T$	tangential direction
$_Z$	in-plane component
$'$	value at representative radius position
$\bar{}$	value normalized with blade radius
$\tilde{}$	instant value at azimuthal positions
$\vec{}$	vector
*	test condition with wind on and motor idle

Introduction

Background

Advances in new electric propulsion technologies renewed interests in the prospect of vertical take-off and landing (VTOL) aircraft. According to Ref. 1, over 200 electric VTOL (eVTOL) manned or unmanned concepts are currently under development. A majority of them uses one or multiple rotors for both lift generation and flight control during VTOL operations.

To fully extract the advantage of eVTOL aircraft, a robust autonomous flight control system is used to manage the transition flight phase between hover and horizontal cruise. Its implementation requires good understanding and precise modeling of the external forces and moments on aircraft. At low airspeed, aerodynamic forces and moments from the proprotor constitute the main part of the vehicle loads.

In pure vertical ascent/descent as well as horizontal cruise, freestream velocity is closely aligned with the proprotor axis. In these situations, flow condition around the proprotor could be treated as axisymmetric. Thanks to this assumption, only thrust force and proprotor torque are generated along the proprotor axis, no lateral force or moment model is required.

For the transition flight phase, the rapid change of trajectory causes a large difference between freestream direction and proprotor axis, which is characterized as proprotor incidence angle α_p in Fig. 1. For proprotor modeling concerns, α_p should be considered independent from aircraft aerodynamic angles. In the aircraft reference frame, aerodynamic angles include angle of attack α_{ac} and side-slip angle β_{ac}: angle of attack α_{ac} is measured from the freestream component in the aircraft symmetric plane to its longitudinal axis; side-slip angle β_{ac} is measured from the freestream component in the aircraft lateral plane to its longitudinal axis. To determine proprotor performance, only one aerodynamic angle is required, the proprotor incidence angle is defined as the angle between freestream direction and proprotor axis. For full aircraft analysis, it is possible to convert α_{ac} and β_{ac} to α_p for each propeller considering its individual orientation respective to the aircraft longitudinal axis. Such conversion is usually trivial and will not be discussed in the current paper.

In axial flow condition, α_p is zero and increases to $\pi/2$ for edgewise flow. For nonzero incidence angles, a proprotor coordinate system is defined in Fig. 2. Freestream V_∞ is projected into two components: V_A along rotation axis and V_Z in rotor disk plane. The proprotor coordinate takes the rotor center as origin, with the x-axis being the rotating axis and the y-axis aligned with V_Z. The y-axis is referred to as the downwind axis.

As a consequence of nonzero incidence angle, axisymmetric assumption is no longer valid. Local velocity and angle of attack for each blade section vary with azimuth position ψ on the rotor disk; therefore, an imbalance of lift and drag forces exists on a blade section over a full revolution. As will be further discussed, lift imbalance creates an in-plane moment n around the downwind axis and drag imbalance causes normal force N along the downwind axis. Furthermore, because blade loading depends quadratically on relative wind speed, the local variations in velocity and angle of attack cause change in disk-averaged thrust T and torque Q in respect to their values at the axial flow condition. The main forces and moments affecting proprotor performance at high incidence are defined in Fig. 2.

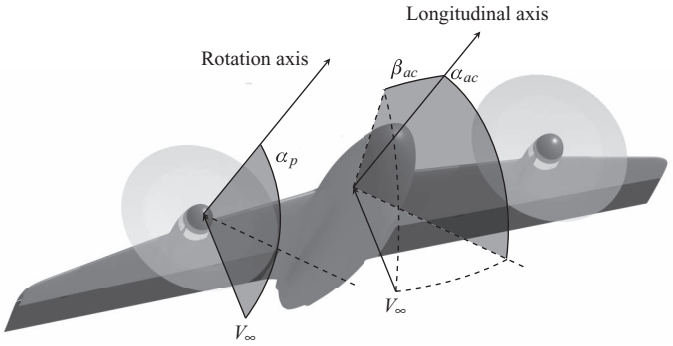

Fig. 1. Definition of aerodynamic angles in proprotor and aircraft reference frames

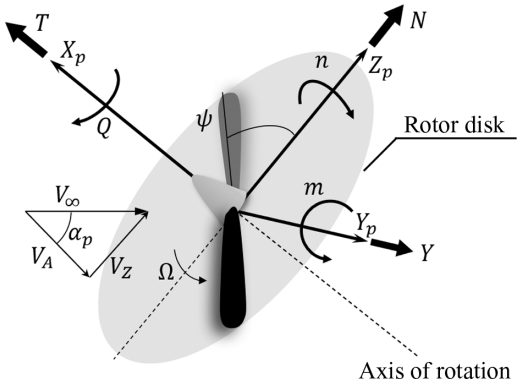

Fig. 2. Aerodynamic loads on a rotor at incidence.

This research concentrates on the development of a computationally efficient method to model the four proprotor aerodynamic forces and moments (T, Q, N, and n) at high incidence, a condition typical during VTOL transition. To keep it computationally efficient, the proprotor loads are given in the explicit form. The model also takes into account proprotor geometry to aid preliminary design requirements.

A review of notable researches in this field is introduced in the next section, followed by a detailed derivation of the mathematical model in analytical form. A dedicated wind-tunnel test for a proprotor with known geometry is documented in the third section, and its main results are used to validate the proposed analytical model. Main findings and comparison with experimental results are presented in the last section.

Literature review

Studies on rotor at nonzero incidence angle first appeared in Refs. 2 and 3. These early results focused on stability issues of fixed-wing aircraft at relatively a small pitch angle. Their methods were based on momentum theory and were linearized by assuming small angles. The resulting methods cannot consider the effect of blade shape on rotor off-axis loads.

Reference 4 and 5 derived an analytic model for propeller off-axis loads. The model considers propellers to be vertical fins having an equivalent side area, and thus propeller planform shape, including chord and pitch angle laws, was considered. The linearized theory showed good agreement for incidence angle up to 20°. A further extension in Ref. 6 attempted to simplify the linear model in Ref. 4 and cover a higher incidence angle range to 65°. However, authors have found that singularities around 90° incidence angle and minor errors in the derivation limited its application.

Various numerical models have also been proposed to treat rotor performance at incidence. The development of a numerical method enabled more detailed analysis based on blade element theory (BET), vortex method, and numerical solution of Navier–Stokes equations. Notable research includes the blade element momentum theory formulated in Ref. 7 and dynamic inflow model for helicopter rotor in Ref. 8. A more recent blade element study in Ref. 9 observed several particular aerodynamic phenomena associated with high incidence flight conditions. A stall delay model and inflow model were determined to be critical in achieving a good correlation with experimental data. Despite the advancements, these numerical methods were relatively costly to be integrated into a full-vehicle optimization routine.

It can be concluded that a more detailed yet computationally efficient approach is of interest for VTOL capable convertible aircraft studies. Evidence appears in recent researches on propeller off-design conditions of unmanned aerial vehicles (UAV). Experimental research in Ref. 10 provided forces and moments measurements over a wide range of incidence angles and freestream speeds on small-scale propellers. A set of the new data-driven parametric model was recently proposed in Ref. 11. The model followed first-principle blade element derivations. Experimental data were needed for training to determine four model parameters. Geometry information was implicitly considered. The model was computational efficient; however, prediction of off-axis loads directly from propeller geometry might be difficult.

In view of past studies, this paper presents an analytic data-driven model with significant advantage in computational efficiency over the current numerical approach. In addition, the model overcomes the constraining hypothesis in conventional momentum methods presented in Refs. 7 and 12, for example, to be better suited for the VTOL transition flight phase. Uniform disk loading is assumed in these theories because they focus on high-speed forward flight helicopters, where induced velocity is of a smaller order of magnitude compared to freestream. This potential error has been mentioned in Refs. 12 and 13. Generally, these theories are applicable to high-speed forward flight ($\alpha_p \approx 90°$).

To present the current research, the model formulation is first introduced in the next section. Proprotor geometry is used to calculate model coefficients, and axisymmetric thrust and power curves, which are easy to be predicted theoretically or to be obtained experimentally, are needed as a base case. In the following section, results from a small-scale proprotor test are presented to validate the current model. The comparison demonstrates sufficient capability in current model to estimate asymmetric force and moment while power consumption is usually underestimated at high incidence conditions. The proposed method is sufficiently accurate and has a significant advantage in computational efficiency and thus is suitable for preliminary vehicle design or real-time applications.

Theoretical Analysis and Analytic Model Derivations

Blade element analysis

To better elucidate the formulation of analytical models, it is imperative to understand the main aerodynamic loads present on the proprotor blade. The production of these forces and moments will be briefly introduced in this section using blade element analysis. The axial flight condition will first be analyzed and then expanded to conditions at nonzero incidence.

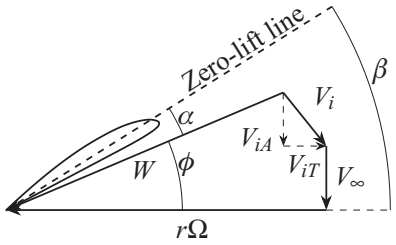

Fig. 3. Blade section in axial flow

Axial flight condition. A proprotor is considered to be immersed in uniform freestream whose direction is in the axis of rotation. Under such an assumption, each infinitesimal blade section at the same radius r from the hub should encounter identical flow conditions, and thus the flowfield is axisymmetric. The analysis will be limited to low-speed condition; hence, incompressible flow is assumed.

Consider a blade section along the circumference at radius r from the axis of rotation. Its orientation is determined relative to the rotor disk plane, which is represented by the horizontal lines in Fig. 3. The local pitch angle β is defined as the angle between the sectional zero-lift line and the rotor disk plane, as in Ref. 14.

As the blade rotates, there are two major components of imposed flow velocity in Fig. 3. First, the freestream velocity V_∞ and second circumferential rotation velocity Ωr.

Besides V_∞ and Ωr, velocity V_i induced by the production of thrust and torque on the proprotor blade is also depicted in Fig. 3. To produce forward thrust, momentum must be added to the fluid in the axial direction, thus creating an incremental velocity component in the rotation axis V_{i_A}. To sustain proprotor rotation, a torque must be supplied and similarly a tangential flow component V_{i_T} is induced due to the exchange of angular momentum.

The local effective wind velocity W is the vector sum of all the velocity components. The angle between W and proprotor disk plane is inflow angle ϕ. The difference between blade pitch and inflow angle gives the local angle of attack $\alpha = \beta - \phi$.

The lift and drag of the blade section can be resolved in directions perpendicular and parallel to the effective wind, respectively, taking chord Reynolds number and local angle of attack into account. They can then be transferred into sectional thrust and torque.

$$\begin{aligned} dT &= \tfrac{1}{2}\rho\,[W(r)]^2\,c(r)\,[C_L(r)\cos\phi(r) - C_D(r)\sin\phi(r)]\,dr \\ dQ &= \tfrac{1}{2}\rho\,[W(r)]^2\,c(r)\,[C_L(r)\sin\phi(r) + C_D(r)\cos\phi(r)]\,r\,dr \end{aligned} \tag{1}$$

Proprotor thrust and torque can be found by integrating Eq. (1) along the blade radius. Because of the axisymmetric flow condition, the analysis is independent of blade azimuthal position. The total thrust and torque are given in Eq. (2).

$$\begin{aligned} T &= \pi\rho R^2 \int_{\bar{r}_0}^{1} [W(\bar{r})]^2\,\sigma(\bar{r})\,[C_L(\bar{r})\cos\phi(\bar{r}) - C_D(\bar{r})\sin\phi(\bar{r})]\,d\bar{r} \\ Q &= \pi\rho R^3 \int_{\bar{r}_0}^{1} [W(\bar{r})]^2\,\sigma(\bar{r})\,[C_L(\bar{r})\sin\phi(\bar{r}) + C_D(\bar{r})\cos\phi(\bar{r})]\,\bar{r}\,d\bar{r} \end{aligned} \tag{2}$$

where $\sigma = \frac{N_b c}{2\pi R}$ is proprotor local solidity. Typically, the thrust and torque are normalized according to air density ρ, proprotor tip speed ΩR, and

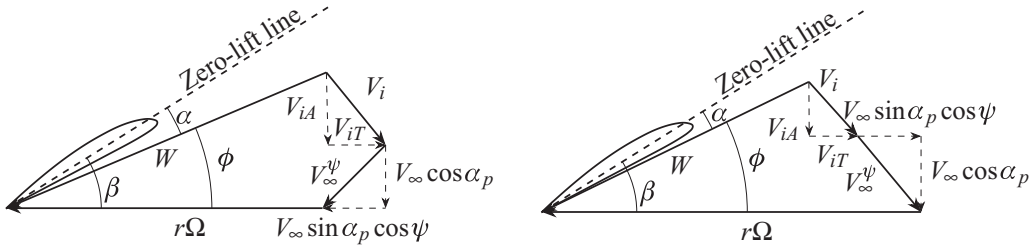

(a) Advancing blade **(b) Retreating blade**

Fig. 4. Flow directions of advancing and retreating blade sections.

disk area $S_p = \pi R^2$.

$$C_T = \frac{T}{\rho (\Omega R)^2 S_p} = \int_{\bar{r}_0}^1 \left[\frac{W(\bar{r})}{\Omega R}\right]^2 \sigma(\bar{r}) [C_L(\bar{r}) \cos\phi(\bar{r}) - C_D(\bar{r}) \sin\phi(\bar{r})] d\bar{r}$$

$$C_P = \frac{Q\Omega}{\rho (\Omega R)^3 S_p} = \int_{\bar{r}_0}^1 \left[\frac{W(\bar{r})}{\Omega R}\right]^2 \sigma(\bar{r}) [C_L(\bar{r}) \sin\phi(\bar{r}) + C_D(\bar{r}) \cos\phi(\bar{r})] \bar{r} d\bar{r} \quad (3)$$

Nonzero incidence angle. At nonzero α_p, freestream can be broken down into an axial component $V_A = V_\infty \cos\alpha_p$ and $V_Z = V_\infty \sin\alpha_p$ in the rotor disk plane. Component V_A has a reduced freestream effect in axial direction, and V_Z causes a variation of flow condition as a function in blade azimuthal position ψ.

Blade element analysis for nonzero α_p follows the same fashion except that most flow components vary with ψ, which is defined to be zero when the blade is aligned with the downwind direction.

Flow conditions for a blade section on two sides of the proprotor are illustrated in Fig. 4.

On the advancing side of the proprotor, where $0 < \psi < \pi$, the in-plane projection is in the same direction of blade rotation. Its effect is to increase local relative wind speed and angle of attack. The opposite is true for the retreating side, where $\pi < \psi < 2\pi$. As a consequence, the magnitude and direction of local relative wind for each blade section are now functions of $\bar{r}$ and ψ. Sectional lift and drag coefficients also depend on ψ. Therefore, the mean thrust and power coefficients become double integration in both $\bar{r}$ and ψ.

$$C_T = \int_0^{2\pi} \int_{\bar{r}_0}^1 \left[\frac{W(\bar{r},\psi)}{\Omega R}\right]^2 \sigma(\bar{r}) [C_L(\bar{r},\psi) \cos\phi(\bar{r},\psi) - C_D(\bar{r},\psi) \sin\phi(\bar{r},\psi)] d\bar{r} d\psi$$

$$C_P = \int_0^{2\pi} \int_{\bar{r}_0}^1 \left[\frac{W(\bar{r},\psi)}{\Omega R}\right]^2 \sigma(\bar{r}) [C_L(\bar{r},\psi) \sin\phi(\bar{r},\psi) + C_D(\bar{r},\psi) \cos\phi(\bar{r},\psi)] \bar{r} d\bar{r} d\psi \quad (4)$$

The imbalance of sectional forces results in axisymmetric normal force and in-plane moment in a global sense. The normal force can be explained by taking the net contribution of tangential force in the downwind axis, as shown in Eq. (5).

$$C_N = \frac{N}{\rho (\Omega R)^2 S_p} = \frac{1}{2\pi} \int_0^{2\pi} \sin\psi \int_{\bar{r}_0}^1 \left[\frac{W(\bar{r},\psi)}{\Omega R}\right]^2 \sigma(\bar{r}) [C_L(\bar{r},\psi) \sin\phi(\bar{r},\psi) + C_D(\bar{r},\psi) \cos\phi(\bar{r},\psi)] \bar{r} d\bar{r} d\psi \quad (5)$$

The in-plane moment is obtained by taking the moment of thrust force around the downwind axis in Eq. (6).

$$C_n = \frac{n}{\rho (\Omega R)^2 S_p R} = \frac{1}{2\pi} \int_0^{2\pi} \sin\psi \int_{\bar{r}_0}^1 \left[\frac{W(\bar{r},\psi)}{\Omega R}\right]^2 \sigma(\bar{r}) [C_L(\bar{r},\psi) \cos\phi(\bar{r},\psi) - C_D(\bar{r},\psi) \sin\phi(\bar{r},\psi)] \bar{r} d\bar{r} d\psi \quad (6)$$

Thrust and power model

Proprotor thrust and power coefficients have been well studied for axisymmetric conditions, a semiempirical estimation for an arbitrary proprotor can be found in Ref. 15. For fixed-pitch configuration at zero incidence angle, the coefficients mainly depend on proprotor tip speed ratio $\lambda_\infty = \frac{V_\infty}{\Omega R}$, which is the ratio of freestream speed and the proprotor tip speed. Reference 15 suggested a linear approximation for thrust and power coefficients :

$$C_T = K\pi \bar{r}' \sigma' \cos\beta' (\lambda_{\infty_{0T}} - \lambda_\infty) \quad (7)$$

$$C_P = K(\pi \bar{r}')^2 \sigma' \sin\beta' (\lambda_{\infty_{0P}} - \lambda_\infty) \quad (8)$$

where K is an empirical constant and $\bar{r}'$ is the position of the representative section in percentage radius (generally 75%). The solidity σ' and pitch angle β' are evaluated at the representative section. Two important parameters are $\lambda_{\infty_{0T}}$ and $\lambda_{\infty_{0P}}$, they are the tip speed ratios where the thrust and power coefficients reach zero, respectively. They can be found graphically or estimated empirically in Ref. 15.

For a nonzero incidence angle, two additional ratios are used to describe freestream condition: rotor climb inflow ratio $\lambda_c = \frac{V_\infty \cos\alpha_p}{\Omega R}$ is taken from the rotation axis and rotor advance ratio $\mu = \frac{V_\infty \sin\alpha_p}{\Omega R}$ is taken from the flow component parallel to disk plane. For zero incidence angle, $\lambda_\infty = \lambda_c$ and $\mu = 0$.

Reference 6 proposed an analytical approach to apply a high incidence angle correction factor to thrust and power coefficients in an effective axisymmetric condition with the same climb inflow ratio λ_c. The correction factor is a function of both climb inflow ratio λ_c and advance ratio μ.

$$\eta_T = C_T(\mu, \lambda_c) / C_T(0, \lambda_c) \quad (9)$$

$$\eta_P = C_P(\mu, \lambda_c) / C_P(0, \lambda_c) \quad (10)$$

This method proves to be sufficiently accurate even for high incidence angles, and it forms the basis for off-axis efforts modeling, and thus is briefly presented in this section.

Local advance ratio. As seen in the blade element analysis in off-axis condition, inflow angle ϕ is a function in ψ. It reaches a minimum at $\psi = \pi/2$ and a maximum at $\psi = 3\pi/2$. This variation of inflow angle ϕ

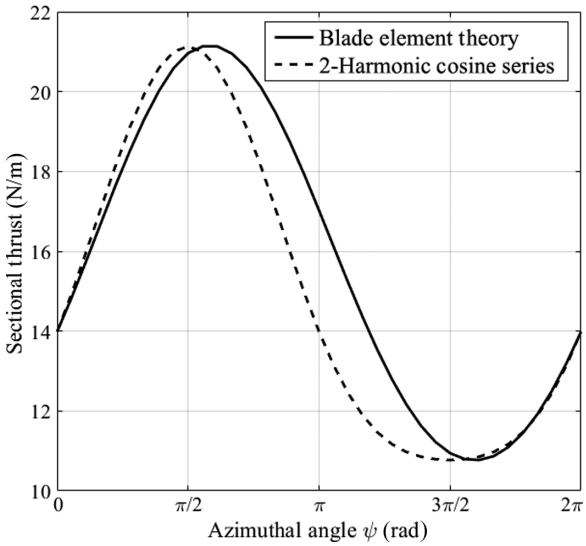

Fig. 5. Comparison between a blade element solution of thrust variation and cosine approximation.

can be characterized by local speed ratio at representative blade section.

$$\lambda_{\text{local}} = \frac{\lambda_c}{1 + \mu \sin\psi/\bar{r}'} \tag{11}$$

We also denote three particular local advance ratios at $\psi = 0, \pi/2$, and $3\pi/2$.

$$\lambda_0 = \lambda_c \tag{12}$$

$$\lambda_{\min} = \frac{\lambda_c}{1 + \mu/\bar{r}'} \tag{13}$$

$$\lambda_{\max} = \frac{\lambda_c}{1 - \mu/\bar{r}'} \tag{14}$$

From linear approximations in Ref. 15, the local thrust coefficient can be related to freestream dynamic pressure and local advance ratio.

$$C_T(\psi) = K\pi\bar{r}'\sigma\cos\beta'(\lambda_{\infty_{0T}} - \lambda_{\text{local}})\left(\frac{\lambda_c}{\lambda_{\text{local}}}\right)^2 \tag{15}$$

High incidence angle corrections for thrust and power. Variations in blade angle of attack and dynamic pressure induce periodic load variation in ψ, which could be approximated by a 2-harmonic cosine series as in Ref. 6.

$$\tilde{C}_T(\psi) = A_0 + A_1\cos\left(\psi - \frac{\pi}{2}\right) + A_2\cos(2\psi - \pi) \tag{16}$$

The curve notably has several characteristic points:

$$\begin{aligned} C_{T_{\text{base}}} &= A_0 - A_2\psi = 0 \\ C_{T_{\max}} &= A_0 + A_1 + A_2\psi = \pi/2 \\ C_{T_{\min}} &= A_0 - A_1 + A_2\psi = 3\pi/2 \end{aligned} \tag{17}$$

This approximation, though not exact, is a reasonable description of sectional thrust variation, as seen in Fig. 5. The curve depicts thrust variation at different azimuthal positions of one blade section situated at 76%R for a constant chord proprotor with NACA0012 airfoil (see Ref. 16 for details). The analysis was performed at a typical condition with moderate tip speed ratio $\lambda_\infty = 0.14$ and medium incidence $\alpha_p = \pi/4$.

The solid line was obtained by performing blade element analysis with a dynamic inflow model, interested readers could find more detail regarding the model in Ref. 8. The dashed line is the 2-harmonic cosine series approximation by using the characteristic points calculated from blade element theory. The estimation is reasonable for downwind blade where $\psi \in [0, \pi/2) \cup (3\pi/2, 2\pi)$, while the upwind blade thrust is underestimated. The difference is caused by variation of induced velocity in the upwind part, where upwash tends to increase the local angle of attack for an upstream blade.

The averaged thrust within one revolution can be represented by thrust condition at characteristic points.

$$\begin{aligned} C_T &= \frac{1}{2\pi}\int_0^{2\pi}\tilde{C}_T(\psi)\,d\psi \\ &= \frac{1}{2\pi}\int_0^{2\pi}A_0 + A_1\cos\left(\psi - \frac{\pi}{2}\right) + A_2\cos(2\psi - \pi)\,d\psi \\ &= A_0 = \frac{1}{4}(2C_{T_0} + C_{T_{\min}} + C_{T_{\max}}) \end{aligned} \tag{18}$$

Assume the maximal, mean, and minimal thrust coefficients correspond to the minimal, mean, and maximal speed ratios, respectively.

$$\begin{aligned} C_{T_{\max}} &= K\pi\bar{r}'\sigma\cos\beta'(\lambda_{\infty_{0T}} - \lambda_{\min})(\lambda_c/\lambda_{\min})^2 \\ C_{T_0} &= K\pi\bar{r}'\sigma\cos\beta'(\lambda_{\infty_{0T}} - \lambda_0) \\ C_{T_{\min}} &= K\pi\bar{r}'\sigma\cos\beta'(\lambda_{\infty_{0T}} - \lambda_{\max})(\lambda_c/\lambda_{\max})^2 \end{aligned} \tag{19}$$

Substitute the local speed ratios from Eqs. (12)–(14) and insert Eq. (19) into Eq. (18), the averaged thrust coefficient at climb inflow ratio λ_c and advance ratio μ can be obtained.

$$C_T(\mu, \lambda_c) = K\pi\bar{r}'\sigma\cos\beta'\left[\lambda_{\infty_{0T}} - \lambda_c + \frac{\lambda_{\infty_{0T}}}{2}\left(\frac{\mu}{\bar{r}'}\right)^2\right] \tag{20}$$

Notice that without the last term, Eq. (20) is identical to the thrust at effective axisymmetric condition. Divided by the thrust coefficient at the corresponding axisymmetric condition, an expression for the thrust correction factor at the high incidence angle can be resolved.

$$\eta_T = 1 + \frac{(\mu/\bar{r}')^2}{2(1 - \lambda_c/\lambda_{\infty_{0T}})} \tag{21}$$

The correction factor for the power coefficient can similarly be found.

$$\eta_P = 1 + \frac{(\mu/\bar{r}')^2}{2(1 - \lambda_c/\lambda_{\infty_{0P}})} \tag{22}$$

A final correction to thrust and power coefficients is added in Ref. 6 to make them consistent with analysis of helicopter rotor in the forward flight condition is detailed in Ref. 17. The second term in thrust and power correction factors is multiplied by a geometry term $\delta(\mu, \lambda_c)$, which also varies with incidence angle.

$$\begin{aligned} \delta(\mu, \lambda_c) = \frac{3}{2}\cos\beta'\Bigg[1 + \frac{\sigma'}{\tan\beta'}\left(1 + \sqrt{1 + \frac{2\tan\beta'}{\sigma'}}\right) \\ \times\left(1 - \frac{\lambda_c}{\sqrt{\lambda_c^2 + \mu^2}}\right)\Bigg] \end{aligned} \tag{23}$$

The final thrust and power high incidence correction factors are given in Eqs. (24)and (25):

$$\eta_T = 1 + \frac{(\mu/\bar{r}')^2}{2(1 - \lambda_c/\lambda_{\infty_{0T}})}\delta(\mu, \lambda_c) \tag{24}$$

$$\eta_P = 1 + \frac{(\mu/\bar{r}')^2}{2(1 - \lambda_c/\lambda_{\infty_{0P}})}\delta(\mu, \lambda_c) \tag{25}$$

Off-axis loads model

Besides the increase in thrust and power at high α_p, extra off-axis efforts C_N and C_n appear as a result of nonuniform blade loading.

An analytical approach was produced as a linear approximation for small α_p in Refs. 4 and 5. Reference 6 later extended the estimation to high incidence cases. The normal force and in-plane moment were modeled as ratios to their respective gradient at zero incidence angle, which were obtained using the theory in Ref. 4. Reference 6 derived these ratios to be $\tan\alpha_p$, which is actually incorrect. The error results in significant overestimation at high α_p and singularity at $\alpha_p = \pi/2$.

The theory in Ref. 4 for off-axis effort gradients at small incidence is presented in this section first in a form suitable for low-speed/hover condition. A correct evaluation of normal force and in-plane moment in relation to their gradients at zero incidence is then derived. Several results in comparison with classical theories will follow.

Gradient of off-axis efforts at zero incidence angle. The theory for normal force and in-plane moment gradients at small incidence angle has been well expressed in Ref. 5. The gradients are closed form solutions obtained by analysis of deflected momentum through the analogy of a vertical fin having equal area as the projected area of proprotor blades perpendicular to the rotor disk. In the expressions, the geometry of the proprotor blade was taken into consideration. Although the theory will only be briefly introduced and readers should refer to the original publication for detailed derivation, there are two incentives to present it here again: (1) To remind readers of the results for later usage; (2) the original theory was expressed for high-speed cruise conditions, while a form more suitable for low-speed/hover conditions is presented here.

The gradients are expressed in Eqs. (26) and (27) with all velocity terms normalized by ΩR, and dynamic pressure terms by $\frac{1}{2}\rho(\Omega R)^2$, which is more appropriate for low-speed/hover conditions.

$$\left.\frac{\partial C_N}{\partial \alpha_p}\right|_{\alpha_p=0} = \frac{1}{2\pi^2}\frac{k_s f(\lambda_i)\sigma I_1}{\frac{I_1}{I_1-\Delta}+k_a\sigma I_1} \tag{26}$$

$$\left.\frac{\partial C_n}{\partial \alpha_p}\right|_{\alpha_p=0} = \frac{1}{\pi^2}\frac{k_s f(\lambda_i) m}{1+k_a\sigma(I_1-\Delta)} \tag{27}$$

where λ_i is the induced inflow ratio $\frac{V_i}{\Omega R}$. k_s and k_a are the spinner factor and the sidewash factor taken as constants ($k_s = 1.14$ and $k_a = 0.4$) in the current study, as suggested in Ref. 4. Their analytical definitions can be found in Ref. 4.

The function $f(\lambda_i)$ is the effect of induced velocity V_i on the dynamic pressure at proprotor disk compared to $\frac{1}{2}\rho(\Omega R)^2$, defined in Eq. (28).

$$f(\lambda_i) = \frac{\pi^{\frac{3}{2}}\lambda_\infty^{\frac{1}{2}}(\lambda_\infty+\lambda_i)[\lambda_\infty(\lambda_\infty+\lambda_i)+(\lambda_\infty+2\lambda_i)^2]}{\lambda_\infty^2+(\lambda_\infty+2\lambda_i)^2} \tag{28}$$

For other quantities in Eqs. (26) and (27), we first introduce three integrations based on proprotor blade geometry.

$$I_1 = \frac{3}{4}C_{L_\alpha}\int_{\bar{r}_0}^{1}\frac{c}{c_{0.75R}}\sin\beta' d\bar{r} \tag{29}$$

$$I_2 = \frac{3}{4}C_{L_\alpha}\int_{\bar{r}_0}^{1}\frac{c}{c_{0.75R}}\cos\beta'\bar{r} d\bar{r} \tag{30}$$

$$I_3 = \frac{3}{4}C_{L_\alpha}\int_{\bar{r}_0}^{1}\frac{c}{c_{0.75R}}\frac{\cos^2\phi}{\sin\phi}\bar{r}^2 d\bar{r} \tag{31}$$

where the mean lift line slope C_{L_α} was approximated as $0.95\times 2\pi$ in Ref. 5.

Terms Δ and m are defined with these geometry integrals.

$$\Delta = \frac{(\sigma I_2 - 2\lambda_i)(\sigma I_2 + 4\lambda_i)}{\sigma(1+\sigma I_2)} \tag{32}$$

$$m = \frac{\sigma I_2 + 4\lambda_i}{2(1+\sigma I_3)} \tag{33}$$

Off-axis efforts at high incidence. The off-axis effort gradients calculated from Ref. 4 agree with various experimental data for incidence angle of up to 20°. Linearity however does not hold for high incidence angles, and the change in local dynamic pressure and flow angle must be taken into consideration. In this section, a formulation of off-axis efforts at high incidence is derived in detail for normal force. Expression for the in-plane moment can be derived in a similar procedure.

The normal force N is a result of averaged tangential force projected in downstream direction. The integration of the moment generated by tangential force at proprotor hub amounts to proprotor torque. From Eq. (8), the local torque can be expressed in terms of local advance ratios.

$$\tilde{Q}(\psi) = \frac{4\rho(\Omega R)^2 S_p R}{\pi^2} K\sigma\sin\beta' A(\psi) B(\psi) \tag{34}$$

where factor $A(\psi)$ estimates the influence of local dynamic pressure change and factor $B(\psi)$ includes the effect of local inflow angle variation implicitly. The two factors are calculated from Eqs. (35) and (36):

$$A(\psi) = (1+\mu\sin\psi/\bar{r}')^2 \tag{35}$$

$$B(\psi) = \lambda_{\infty_{0P}} - \frac{\lambda_c}{1+\mu\sin\psi/\bar{r}'} \tag{36}$$

The tangential force $\tilde{F}_T$ can be estimated by dividing the local torque by the representative radius r', and thus is proportional to torque $\tilde{Q}(\psi)$. For clarity in the following derivations, proportional constants are neglected.

$$\tilde{F}_T(\psi) = \frac{\tilde{Q}(\psi)}{r'} \propto A(\psi) B(\psi) \tag{37}$$

Expand Eq. (37) and rearrange terms, the tangential force expression can be reformulated as Eq. (38).

$$\tilde{F}_T(\psi) \propto (\lambda_{\infty_{0P}} - \lambda_c) + \left(\frac{\mu}{\bar{r}'}\right)(2\lambda_{\infty_{0P}} - \lambda_c)\sin\psi + \left(\frac{\mu}{\bar{r}'}\right)^2\lambda_{\infty_{0P}}\sin\psi \tag{38}$$

Assume that the averaged normal force N is proportional to the mean of integrated tangential force projected in the downwind direction in one revolution. Constant and second-order terms in Eq. (38) are zero after integration. The normal force is written as a function in α_p and λ_∞ in Eq. (40), as it makes the form easier to apply the force and moments gradients in Eqs. (26) and (27).

$$N(\alpha_p, \lambda_\infty) \propto \frac{1}{2\pi}\int_0^{2\pi}\tilde{F}_T(\psi)\sin\psi d\psi \tag{39}$$

$$\propto (2\lambda_{\infty_{0P}} - \lambda_\infty\cos\alpha_p)\lambda_\infty\sin\alpha_p \tag{40}$$

Differentiate Eq. (40) with respect to incidence angle α_p and evaluate the normal force gradient at zero incidence.

$$\left.\frac{dN(\alpha_p,\lambda_\infty)}{d\alpha_p}\right|_{\alpha_p=0} \propto \lambda_\infty(2\lambda_{\infty_{0P}} - \lambda_\infty) \tag{41}$$

Thus the evolution of normal force at high incidence can be evaluated as a ratio to normal force gradient at zero incidence with the same λ_∞.

Fig. 6. 3D printed NACA proprotors.

The resultant relation is a product of $\sin\alpha_p$ and λ_∞ terms.

$$\frac{N(\alpha_p,\lambda_\infty)}{\partial N/\partial\alpha_p(0,\lambda_\infty)} = \frac{2\lambda_{\infty_{0P}} - \lambda_\infty\cos\alpha_p}{2\lambda_{\infty_{0P}} - \lambda_\infty}\sin\alpha_p \tag{42}$$

In a similar manner, the same relation can be obtained for the in-plane moment by using the azimuthal variation of local thrust. The off-axis efforts are expressed as coefficients in Eqs. (43) and (44).

$$C_N = \frac{2\lambda_{\infty_{0P}} - \lambda_\infty\cos\alpha_p}{2\lambda_{\infty_{0P}} - \lambda_\infty}\sin\alpha_p \left.\frac{\partial C_N}{\partial\alpha_p}\right|_{\alpha_p=0,\lambda_\infty} \tag{43}$$

$$C_n = \frac{2\lambda_{\infty_{0T}} - \lambda_\infty\cos\alpha_p}{2\lambda_{\infty_{0T}} - \lambda_\infty}\sin\alpha_p \left.\frac{\partial C_N}{\partial\alpha_p}\right|_{\alpha_p=0,\lambda_\infty} \tag{44}$$

Comparisons with classical theories

The analytical model was compared with classical theories for nonzero incidence angle conditions. These consist of mainly two categories: linear analysis in aircraft stability (Refs. 5, 14, 18) and performance analysis on helicopter lift and drag (Refs. 7, 12, 17). The first category considers proprotor off-axis loads at small incidence ($\alpha_p \approx 0$), while the second category focuses at α_p near $\pi/2$. Models in these two well-studied conditions serve as benchmark of the current analytic model, which is applicable to arbitrary α_p.

A small-scale proprotor with predefined geometry was used in model validation. The proprotor features a constant chord and NACA0012 blade section profile, and thus is referred to as a NACA proprotor. The twist distribution is given as $\beta = \tan^{-1}\frac{C}{\bar{r}}$, where $C = \tan\beta_{\text{tip}}$. The tip blade angle β_{tip} is equal to 20°, as shown in Fig. 6. Tabulated chord and pitch distribution laws with root cutoff can be found in Table B.1 of Appendix B. A physical model was manufactured for the wind tunnel experiment discussed in the next section.

Linearized model for off-axis loads at small incidence. Linearized normal force and in-plane moment models have been used frequently in fixed-wing aircraft researches, since they typically fly at small incidence angle. The original model developed in Ref. 4 is one of these types. A more recent model documented in Ref. 14 and implemented in Ref. 19 will be used as a reference in this section to demonstrate the accuracy of the proposed model at incidence angle below 45°.

The linearized theory was formulated from a blade element approach. The off-axis force and moments were linearized around $\alpha_p = 0$ based on small angle assumptions. The theory also assumes that freestream velocity is small compared to rotor speed ($\lambda_\infty \ll 1$).

Normal force and in-plane moment coefficients are plotted in Figs. 7 and 8, respectively. The linear theory results are plotted in a dashed line, and results from the current nonlinear theory are presented in a solid line. Different markers represent various tip speed ratios.

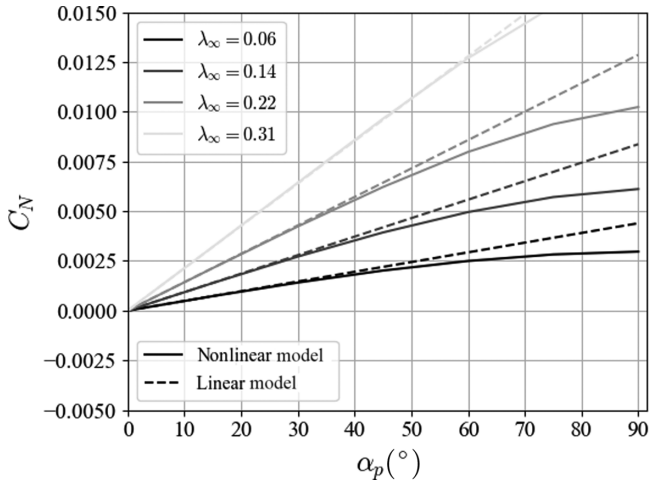

Fig. 7. C_N of a small-scale proprotor versus α_p from theory in Ref. 14 and from current theory.

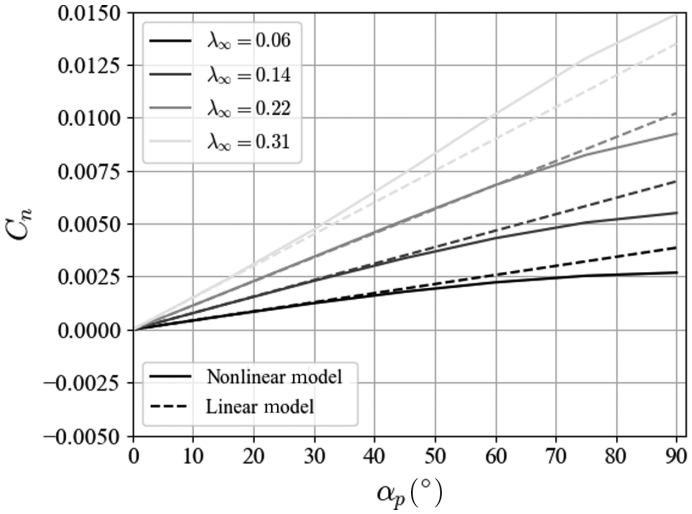

Fig. 8. C_n of a small-scale proprotor versus α_p from theory in Ref. 14 and from current theory.

In Fig. 7, the normal force estimations from both theories are compared. The theory in Ref. 14 underestimates the normal force. The discrepancies appear to reduce with increasing tip speed ratio. For example, at $\lambda_\infty = 0.06$, the linear theory gives a value 53% lower than the nonlinear model at $\alpha_p = 10°$. The difference decreases to 27% at a higher tip speed ratio of 0.31. The linear model evidently could not predict the level-off of normal force at a higher incidence angle, but such discrepancy is not significant in the low incidence angle range.

For in-plane moment estimations presented in Fig. 8, both theories give consistent values for $\lambda_\infty \leq 0.14$. The difference typically does not exceed 20% in the low incidence angle range. At a higher speed ratio, the linear theory starts to underestimate in-plane moment. This is because the assumptions of small angle and low tip speed ratio start to break down.

Helicopter forward flight theory. A comparison with classical helicopter forward flight theory may give further insight into the behavior of current

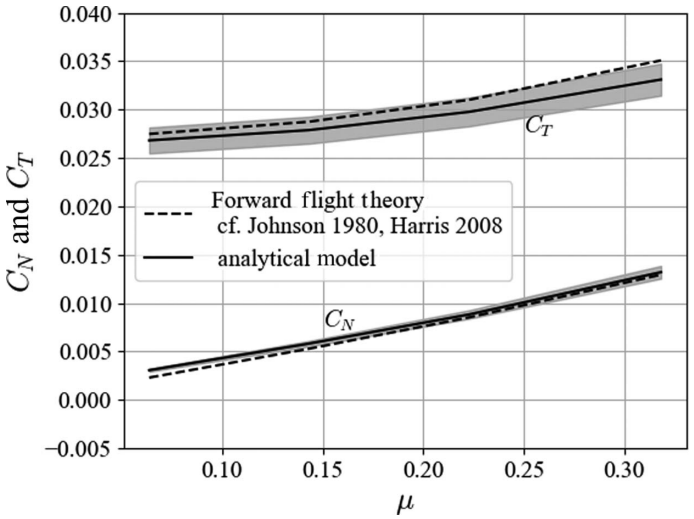

Fig. 9. NACA proprotor thrust and normal force coefficients at various μ.

model at $\alpha_p \approx \pi/2$. A detailed discussion of such analysis can be found in Ref. 12.

The theory is based on a linearized blade element model, small angle assumption on inflow angle, and nonflow-reversal assumption. The latter was validated in Ref. 12 with limitation of $\mu \leq 0.3$. The theory is developed in Ref. 12 for articulated straight high aspect ratio blade. As a result, blade flapping terms were included in the original form. However small-scale proprotors are usually hingeless and rather rigid, and thus the extra terms were omitted.

Extensive reviews from Refs. 20 and 21 further extended the applicable μ range for normal force estimation at higher flight speed. This is also included in the normal force comparison.

From forward flight theory, proprotor thrust, power, and normal force can be directly resolved for $\alpha_p = \pi/2$. Thrust and normal force are compared with the current model in this section.

The thrust and normal force coefficients are presented in Fig. 9 against advance ratio μ. An error band of $\pm 5\%$ is also plotted for each dataset from the current model.

Over the rotor advance ratio range, the prediction of the current model agrees mostly within 5% of the forward flight theory. Both thrust and normal coefficients increase with advance ratio with C_N exhibiting a more linear characteristics.

Classical forward flight theory starts to overestimate thrust coefficient at high advance ratio. Considering the theory's limit of $\mu \leq 0.3$, the overestimated value might be explained by the extension of the flow reversal region. The current model interprets aerodynamic characteristics according to axial proprotor performance (usually obtained by wind tunnel tests), and thus the thrust performance is restricted while no explicit treatment of flow reversal is included.

Classical forward flight theory is in close agreement with the current model in normal force prediction. C_N estimation in classical forward flight theory consists of two parts: induced and profile drag. The first part considers inflow angle variation due to thrust induced flow, while the second part considers contributions due to sectional and radial drag. The agreement in Fig. 9 suggests that influences from both parts have been included in the current model, and the results are quantitatively consistent.

Computational efficiency. One of the major advantage of the analytic model is its computational efficiency. Table 1 illustrates typical order of magnitude of processor time per calculation case for widely used propeller models. The figures were obtained through in-house calculations on similar low Reynolds number proprotor cases over a limited test conditions (Refs. 9, 22, 23).

Table 1. Order of magnitude of CPU time per case for different numerical propeller models

Numerical Method	Level of Resolution	CPU Time order of Magnitude per case (s)
Analytical method (current)	Low	10^{-3}
BEMT (Ref. 9)	Medium	10^{1}
Nonlinear vortex lattice method (Ref. 22)	High	$10^{4} - 10^{6}$
Unsteady Reynolds-averaged Navier–Stokes (RANS) (Ref. 23)	High	10^{7}

According to the table, the current method has a significant advantage over other methods in the preliminary design phase, where the requirement of rapid and robust calculation outweighs solution precision. Its computational efficiency may also benefit further real-time applications. The accuracy of the current model will be further discussed in the following section through comparison of experimental data.

The blade element momentum method is also widely used for propeller design. However, since the axisymmetric flow condition no longer exists, the method must be expanded to calculate solution at each azimuthal angle, hence the increased CPU time compared to a usual axisymmetric case.

Both nonlinear vortex lattice method and unsteady RANS method solve directly wall boundary condition to achieve high-resolution spatial solution. A large amount of calculation is required for sufficient wake development in order to obtain steady-state solution. Therefore, these methods are more suitable for detailed design.

Experimental Studies

To validate the analytical model derived in the previous section, an experimental study was conducted and is presented in this section. The test was performed in low Reynolds number wind tunnel SaBRe at ISAE-Supaero to simulate typical UAV transition flight condition. An in-house manufactured proprotor was used to ensure sufficient geometric information is available to compare experimental results and numerical models.

Test setup

Mounting and measurement system. The measurement system was installed at the ISAE low Reynolds number wind tunnel SaBRe, which is a closed circuit low-turbulence design with a 1.2 m × 0.8 m test section. The wind tunnel is dedicated for micro aerial vehicles research. The propeller–motor assembly was supported by a rotating strut installed from the test section ceiling. The metal strut was driven by an actuator, which allowed 180° rotation around its vertical axis in either direction, simulating variation of incidence angle.

At the lower tip of the strut, a custom-designed five-component balance was mounted both as a structural connection to the propeller–motor assembly and as the load measuring sensor. The balance was not sensitive to axial force along its longitude axis (parallel to the Y_p axis). The installation is chosen to minimize negative impact and its measuring reference frame is discussed in the Data Process section. The motion control was made through a National Instrument PXI-7350 card and data sampling were realized through a PXI-6229 data acquisition card. The

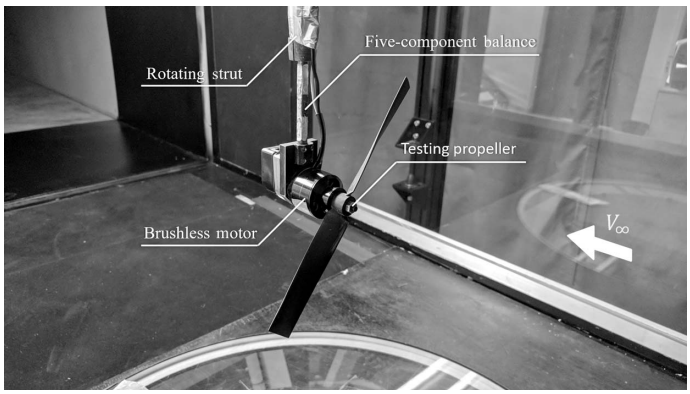

Fig. 10. Propeller test-bench inside the ISAE SaBRe wind tunnel.

Table 2. NACA proprotor test matrix

Tip Speed Ratio λ_∞	Freestream Velocity (m/s)	*Re* at 75%*R*
0.06	3	5.3×10^4
0.14	6	4.7×10^4
0.22	9	4.5×10^4
0.32	10	3.5×10^4

measurement system was mounted on a 12-slot PXI-1050 chassis and managed from Labview software. Experimental data were sampled at 1000 Hz for 10 s period for each test condition, before taking the mean value over the sampling period.

A brushless motor was installed just below the balance loading end, and its rotation axis was determined to be 65 mm lower than the balance center of measurement. In front of the motor, the test proprotor is fixed to the motor spinner. The test bench is shown in Fig. 10.

Tested proprotors. A 9-inch Graupner E-prop was first tested to compare with experiments documented in Ref. 24 for validation. The rotor was operated at 4000 and 4500 RPM with freestream velocity $V_\infty = 6$ m/s. The compared study controlled motor voltage and thus rotation speed varied with incidence angle. Due to excessive vibration below 4000 RPM in current setup, the rotation speeds could not exactly match with published data points.

For model validation, the small-scale NACA proprotor discussed earlier was used since its geometry information is fully accessible. The proprotor was tested at four different tip speed ratios. To achieve the desired λ_∞s, freestream velocity and rotation speed were changed as listed in Table. 2. The reference Reynolds numbers at 75% radius are also listed, which takes into account both freestream and rotation speed.

$$Re_{\bar{r}=0.75} = \frac{V_\infty c}{\nu}\sqrt{1+\left(\frac{0.75}{\lambda_\infty}\right)^2} \tag{45}$$

Data process

Coordinate system. To describe the rotor assembly movement and the transformation from measurement datum to rotor center, a clear definition of the coordinate system is required.

Two coordinates are used. The proprotor frame has its origin O_p at the rotor center, and its orientations are defined in the same way as the analytical model. Therefore, its x-axis coincides with the axis of rotation, and its y-axis points vertically towards the wind tunnel ceiling.

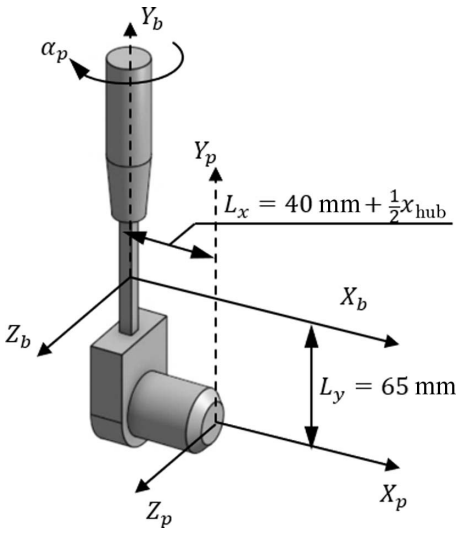

Fig. 11. Balance and proprotor coordinates.

The balance frame has the same orientation as the proprotor system, but its origin is at the measurement datum, which is located $L_y = 0.065$ m above, and $L_x = 0.04$ m behind the base of the rotor mount. The geometric relation between two coordinates is illustrated in Fig. 11.

Rotor thrust T, torque Q, normal force N, in-plane, and pitch moments (n, p) were measured during the test. All rotor aerodynamic loads follow the same definition as in Fig. 2. As mentioned before, the balance used for measurement is only sensitive in five components, namely two forces and three moments along an orthogonal coordinate. Based on Refs. 14, 24, 25, side force Y is negligible and thus the insensitive force axis is aligned with the Y_b-axis.

Compensation for external disturbances. The force measurement from five-component balance contains several external loads apart from proprotor aerodynamic efforts, and thus must be compensated to obtain proprotor loads. The external disturbances are categorized as ffollows:

1) *Static structural load*. It is a result of the gravitational force of the test bench and rotor–motor assembly. This component is measured for each rotor at various incidence angles. In the general form, it contains five components, and its variation with incidence angle is caused by the slight alignment error in balance installation, which is derived in Appendix A.

$$\begin{bmatrix}\vec{F}_0\\ \vec{M}_0\end{bmatrix} = [F_{x0},\, F_{z0},\, M_{x0},\, M_{y0},\, M_{z0}]^T \tag{46}$$

2) *Static aerodynamic load.* The second component is the aerodynamic efforts produced by structures other than the rotor, and is denoted by subscript *aero*. The structure contains mainly cylinder geometries, and thus airflow around those structures should be well separated at testing speeds so that the Reynolds number effect is negligible according to Ref. 26. This component is obtained through two measurements. First, with the rotor uninstalled and $V_\infty = 0$, the motor mass effect F_{m0} and M_{m0} are measured at various incidence angles. The wind tunnel is subsequently run at test speed, and acquisitions of F_m^* and M_m^* are made at corresponding incidence angles. The aerodynamic load is further derived as the difference between these two measurements:

$$\begin{bmatrix}\vec{F}_{aero}\\ \vec{M}_{aero}\end{bmatrix} = \begin{bmatrix}\vec{F}_m^*\\ \vec{M}_m^*\end{bmatrix} - \begin{bmatrix}\vec{F}_{m0}\\ \vec{M}_{m0}\end{bmatrix} \tag{47}$$

To compensate the influence of atmosphere condition on dynamic pressure, the aerodynamic disturbances are further normalized by

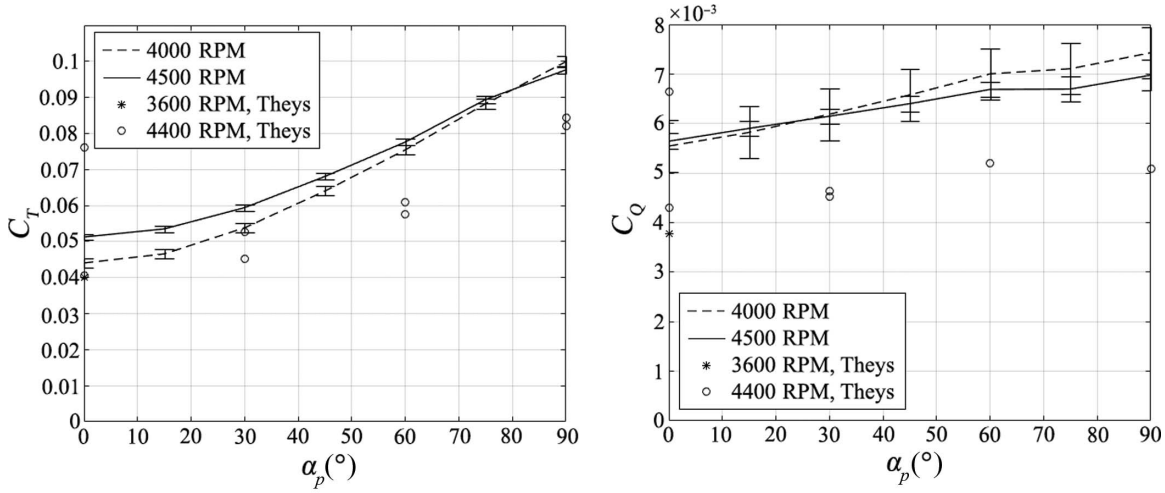

(a) C_T **(b) C_Q**

Fig. 12. Graupner E-prop thrust and torque comparison with Ref. 10.

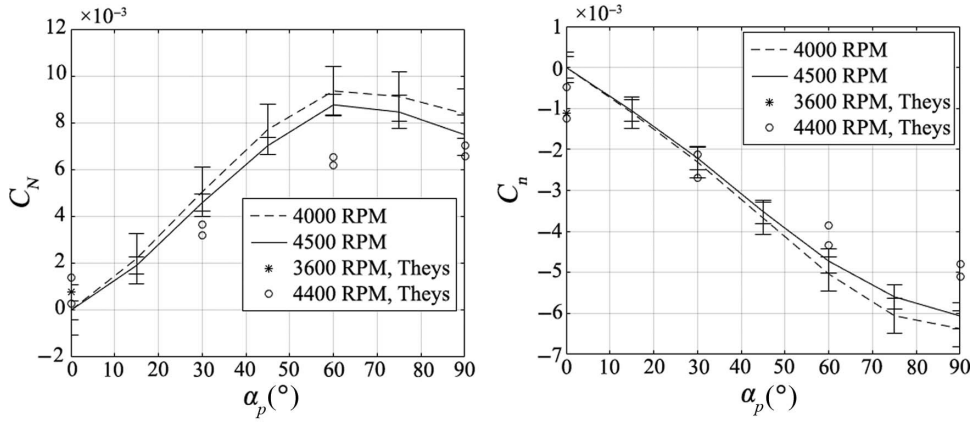

(a) C_N **(b) C_n**

Fig. 13. Graupner E-prop normal force and in-plane moment comparison with Ref. 10.

measured dynamic pressure,

$$\begin{bmatrix} \vec{C}_{F_{aero}} \\ \vec{C}_{M_{aero}} \end{bmatrix} = \frac{2}{\rho V_\infty^2} \begin{bmatrix} \vec{F}_{aero} \\ \vec{M}_{aero} \end{bmatrix} \tag{48}$$

To obtain the rotor aerodynamic forces and moments, those two external disturbances are subtracted from the raw data measured at the measurement datum (F_b^*, M_b^*). The static aerodynamic effects are scaled with measured dynamic pressure before compensation.

$$\begin{bmatrix} \vec{F}_b \\ \vec{M}_b \end{bmatrix} = \begin{bmatrix} \vec{F}_b^* \\ \vec{M}_b^* \end{bmatrix} - \begin{bmatrix} \vec{F}_0 \\ \vec{M}_0 \end{bmatrix} - \frac{1}{2}\rho V_\infty^2 \begin{bmatrix} \vec{C}_{F\,aero} \\ \vec{C}_{M\,aero} \end{bmatrix} \tag{49}$$

To obtain aerodynamic efforts at the rotor center, the compensated forces and moments should be transformed. Following the test bench convention in Fig. 11, the transformation is given in Eq. (50):

$$\begin{bmatrix} \vec{F}_p \\ \vec{M}_p \end{bmatrix} = \begin{bmatrix} 1 & 0 & 0\,0\,0 \\ 0 & 1 & 0\,0\,0 \\ 0 & L_y & 1\,0\,0 \\ 0 & L_x & 0\,1\,0 \\ -L_y & 0 & 0\,0\,1 \end{bmatrix} \begin{bmatrix} \vec{F}_b \\ \vec{M}_b \end{bmatrix} \tag{50}$$

where L_x and L_y are the moment arms from measurement datum to the rotor center in x and y directions, respectively. It is assumed that, after compensation of the mass effect, force in the y direction is negligible.

Test bench validation. The five components obtained from the experiment with Graupner E-prop were compared with values in Ref. 10 at similar rotation speeds, namely thrust T, normal force N, pitching moment p, in-plane moment n, and torque Q. All results are presented for an incidence angle from 0° to $\pi/2$ by an interval of $\pi/6$ and are in the form of nondimensional coefficients.

Figures 12 compares results on thrust and torque. The curves from the ISAE experiment share a similar trend in Ref. 10. At constant rotational speed, the thrust and torque coefficients increase with incidence angle and reach peak value beyond 90°.

An overestimation can be observed when compared with Ref. 10. The discrepancy is highly likely due to the difficulty in matching rotor rotational speed. The rotor in Ref. 10 was controlled by constant voltage input, and thus rotational speed varies slightly with incidence angle. In general, the proprotor rotated at a higher speed than the comparison case, producing larger thrust and torque coefficients.

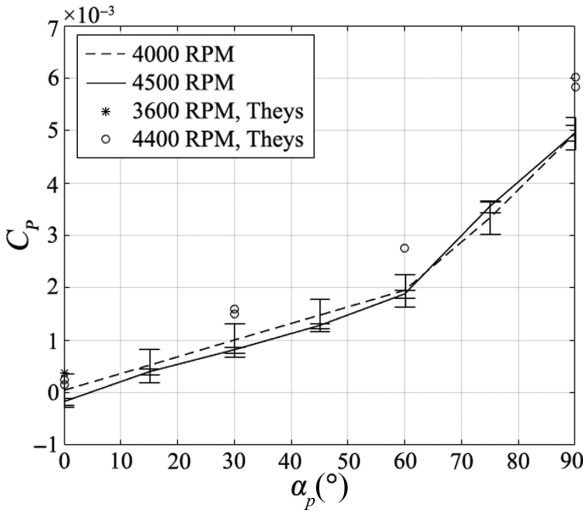

Fig. 14. Graupner E-prop C_p comparison with Ref. 10.

Off-axis forces and moments are presented in Figs. 13 and 14. In Figs. 13, C_N and C_n are presented. The normal force increases with α_p until around $\pi/3$. The measurement from the two experiments agrees well in the tested range.

The in-plane moment measurement largely agrees with data in Ref. 10. The data suggest a quasi-linear increase of in-plane moment till $\pi/3$. The off-axis moment levels off thereafter near $\pi/2$, and a slightly larger value is observed compared to data in Ref. 10.

Figure 14 shows the variation in pitching moment, the supposedly secondary rotor off-axis load. Current measurement is consistent with data in Ref. 10. C_p rises gradually from zero up to around $\pi/3$, where a sharp increase follows.

The origin of pitch moment is likely due to three-dimensional effects when the blades are nearly aligned with the flow direction. It may be further analyzed by comparing phase shift to in-plane moment. The phenomena may be roughly simulated through pressure distribution on a circular wing according to Ref. 13.

The comparison, although not exact, demonstrates the validity of the propeller test bench in the ISAE-SaBRe wind tunnel in providing credible force and moment measurement for a rotor at a high incidence angle. Data acquired from the balance capture principle variation in rotor aerodynamic loads and are accurate for qualitative analysis at the practical range.

Results and Discussion

Validation of the analytical model for thrust and power

Comparisons between the analytical model and the small-scale proprotor test were made for the four tip speed ratios mentioned before. In different markers for the four λ_∞, whose tabulated values can be found in Tables C.1 and C.2 of Appendix C. Theoretical results were extrapolated from coefficients obtained in experiments at zero incidence angle and were plotted in various line styles.

In Fig. 15(a), the thrust coefficient was compared between the analytical model and the experimental data. As expected from classic rotor analysis, at axial conditions, the thrust coefficient decreases with λ_∞. The theoretical value matches exactly with the experimental results since the thrust ratio η_T is unity at zero incidence. With increasing α_p thrust starts to rise gently initially, and more drastically at higher incidence. The variation is larger at a high advance ratio.

The theoretical results agreed reasonably well for all tested conditions, particularly at smaller λ_∞. At around $\alpha_p = \pi/3$, a convergence region can be observed, where all curves seem to pass through. A slight overestimation is observed in low tip-speed ratio $\lambda_\infty = 0.06$.

The comparison for power coefficient is depicted in Fig. 15(b). The nonlinear trend is very similar to that of the thrust coefficient. However, the difference between test data and theoretical results is larger for tip-speed ratio $\lambda_\infty \leq 0.22$. The on-set angle of incidence of deviation decreases with tip-speed ratio, which are at 30° for $\lambda_\infty = 0.22$ and at 15° for $\lambda_\infty = 0.31$. Beyond the on-set incidence angle, theoretical estimation underestimates proprotor torque.

The reason for such deviation is probably due to the effect of the in-plane flow component on the tangential force hypothesis. The 2-harmonic cosine series model used may not be able to capture the exact tangential force under high incidence flow.

By calculating the rotor advance ratio μ at on-set incidence, the model is found to be accurate up to $\mu_{\text{crit}} = 0.08$–0.11.

From the validation, it can be concluded for the tested NACA proprotor, the analytical model applies well for various combinations of λ_∞ and α_p. It also explains well the increasing amplitude of thrust and power coefficients at higher λ_∞. The high incidence thrust and power correction factors in Eqs. (24) and (25) can be rewritten in the form of Eqs. (51) and (52),

$$\eta_T = 1 + \frac{\lambda_\infty(\sin\alpha_p/\bar{r}')^2}{2(1/\lambda_\infty - \cos\alpha_p/\lambda_{\infty_{0T}})}\delta(\alpha_p) \tag{51}$$

$$\eta_P = 1 + \frac{\lambda_\infty(\sin\alpha_p/\bar{r}')^2}{2(1/\lambda_\infty - \cos\alpha_p/\lambda_{\infty_{0P}})}\delta(\alpha_p) \tag{52}$$

The numerator is proportional with λ_∞, while the first term in the denominator reduces. Thus the thrust and power correction factors increase faster with tip speed ratio than a linear function.

Validation of analytical model for off-axis efforts

The normal force coefficient for the NACA proprotor is presented in Fig. 16(a). The model is in good agreement with the experimental results. For small advance ratios, the model mostly resembles the behavior of a sine function, with the largest value obtained at $\pi/2$. For higher tip speed ratios, the λ_∞ term becomes significant and the normal force coefficient is larger than the $\sin\alpha_p$ correction.

There exists a local maximum in the normal force coefficient for each advance ratio. The analytical model is not able to predict this peak, and the theoretical curve overshoots the experimental value after this local maximum.

In Fig. 16(b), the in-plane moment coefficients from the theoretical model and experimental measurement are plotted. The result demonstrated a good trend and agreement for small λ_∞.

For $\lambda_\infty \geq 0.32$, the theoretical value is overestimated. The difference is caused by the linear lift line assumption made at the blade sections. The outer section of the advancing blade is likely to stall at these advance ratios and cannot sustain such a large in-plane moment. As a result, its $\lambda_{\infty_{0T}}$ is significantly larger, which reduces the influence of the λ_∞ term in Eq. (44), indicating less severe blade stall.

Despite the discrepancies between theoretical and experimental results at large λ_∞ and/or high α_p, the model generally provides a reasonable estimation of proprotor behaviors at off-design conditions for a fractional cost of higher order methods.

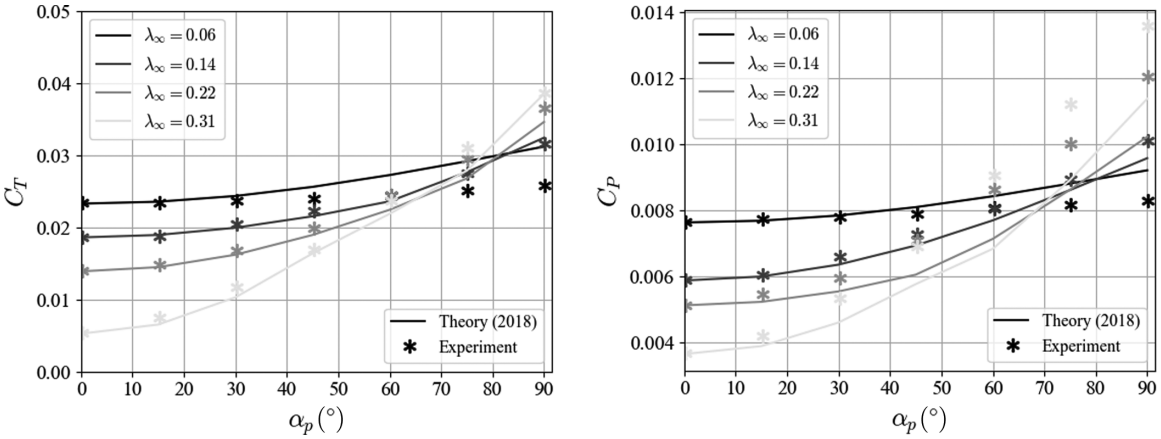

(a) C_T **(b) C_Q**

Fig. 15. NACA proprotor thrust and torque against various λ_∞.

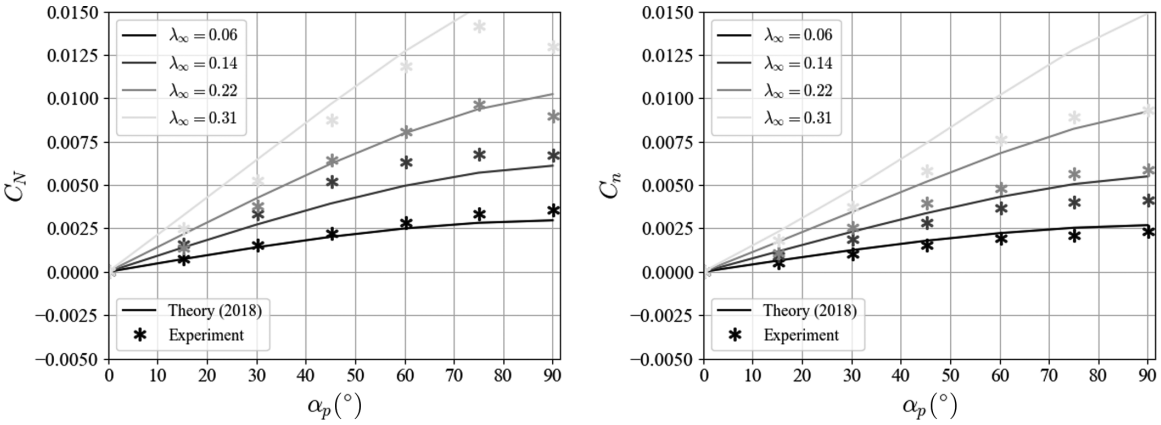

(a) C_N **(b) C_n**

Fig. 16. NACA proprotor normal force and in-plane moment against various λ_∞.

Conclusions

An analytical model was derived, benchmarked, and validated to estimate proprotor thrust, power, normal force, and in-plane moment at nonzero incidence angle. Assumptions typical for the transition flight phase were made to keep the model in closed and tractable form. Blade element theory and representative blade section analysis were used to include influences of proprotor geometry. In light of the studies available, the current model offers a computationally efficient tool over incidence angles between 0 to $\pi/2$. The model is suitable for preliminary design or potentially used as surrogate model for real-time applications.

The accuracy of the model was studied with both classical theories in specific α_p conditions and experimental data over the full α_p range. Analysis confirms the model includes principle aerodynamic effects, including both induced and profile drag components. The agreement with test data within the transition flight phase is desirable. Limitation of the model exists for power estimation at or above rotor advance ratio $\mu = 0.08$–0.11, although such condition appears to be extreme for practical transition flight. For equilibrium transition in constrained space, optimized aircraft would not encounter such condition due to high energy consumption.

Although the current model is able to predict proprotor performance over a wide range of flight conditions, limitations still exist for certain flight regimes of interest. The Backflow condition at moderate descent speed may require analysis for $\alpha_p > \pi/2$, as well as dynamic aerodynamic efforts encountered in gusty conditions or during rapid maneuvers. Furthermore, geometry modifications such as swept angle of some low-noise proprotor designs may be studied.

Acknowledgments

The research was conducted under the industrial agreement of training through research (CIFRE) financed by the Delair company and the French national association of research and technology (ANRT). The authors would like to extend their thanks to the technicians of ISAE-SUPAERO for their technical support and assistance during the wind tunnel campaign, in particular: Mr. Rémy Chanton and Mr. Henri Dedieu for the design and installation of the rotor-mounting system, and Mr. Sylvain Belliot for rotor manufacture.

Appendix A: Static Mass Error

Due to the displacement between the balance and motor–propeller center of mass, there exists a static error in the force and moment measurement. Furthermore, small inclination of the support mast introduces a dependence on the proprotor incidence angle. A simplified free-body diagram is shown Fig. A1 for the test assembly with exaggerated inclination.

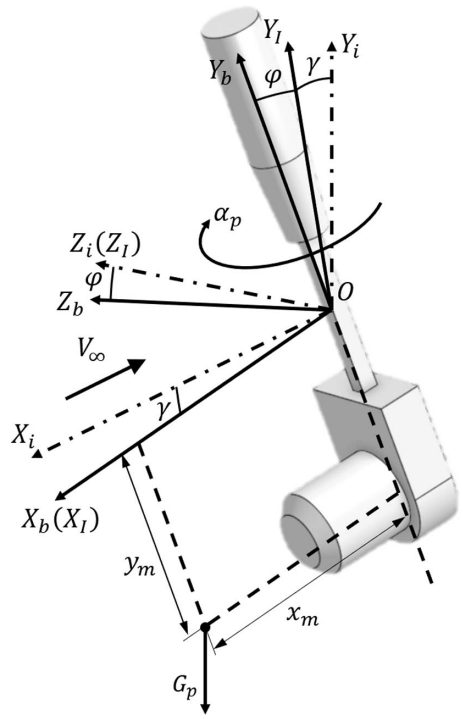

Fig. A1. Definition of balance inclinations.

Table B1. NACA proprotor geometry

Relative Radius r'	Relative Chord c'	Pitch Angle (°)
0.112	0.299	52.099
0.149	0.299	51.429
0.186	0.299	50.570
0.223	0.299	49.521
0.260	0.299	48.284
0.297	0.299	46.857
0.334	0.299	45.241
0.371	0.299	43.436
0.408	0.299	41.441
0.445	0.299	39.258
0.482	0.299	37.041
0.519	0.299	35.028
0.556	0.299	33.198
0.593	0.299	31.531
0.630	0.299	30.008
0.667	0.299	28.614
0.704	0.299	27.334
0.741	0.299	26.155
0.778	0.299	25.068
0.815	0.299	24.062
0.852	0.299	23.130
0.889	0.299	22.264
0.926	0.299	21.457
0.963	0.299	20.704
1.000	0.299	20.000

Three coordinates are depicted in the diagram: (1) ground-fixed frame $OX_iY_iZ_i$, (2) intermediate frame $OX_IY_IZ_I$, and (3) balance body frame $OX_bY_bZ_b$ as introduced before. The motor–propeller center of mass is assumed to be located at x_m and y_m in body frame.

Primary structural deformations are determined to be the inclination of balance frame's Y_b and Z_b axes. The diagram below defines the deformations as two angles φ and γ.

The derivation will consider $\alpha_p = 0$ as the baseline case, where, for $\varphi = \gamma = 0$, X_b axis is parallel to the opposite freestream direction. From the baseline case, the frame first rotates angle γ around the Z_i axis to become intermediate frame $OX_IY_IZ_I$. Then the frame further rotates an angle φ around the X_I axis to reach body frame $OX_bY_bZ_b$. Finally, the body axis rotates around its Y_b axis for different incidence angles α_p.

In ground-fixed frame, the motor–propeller assembly gravity force G_p lies opposite to Y_i axis.

$$\vec{F}_0^i = [0 \ -G_p \ 0]^T$$

To obtain the force components in the body axis, the force in the ground-fixed frame is multiplied by three rotation matrices in order: (1) γ around Z, (2) φ around X, and (3) $-\alpha_p$ around Y. The resultant static force error can be found below:

$$\begin{aligned}\vec{F}_0^b &= \begin{bmatrix}\cos\alpha_p & 0 & -\sin\alpha_p \\ 0 & 1 & 0 \\ \sin\alpha_p & 0 & \cos\alpha_p\end{bmatrix}\begin{bmatrix}1 & 0 & 0 \\ 0 & \cos\varphi & -\sin\varphi \\ 0 & \sin\varphi & \cos\varphi\end{bmatrix} \\ &\times \begin{bmatrix}\cos\gamma & -\sin\gamma & 0 \\ \sin\gamma & \cos\gamma & 0 \\ 0 & 0 & 1\end{bmatrix}\begin{bmatrix}0 \\ -G_p \\ 0\end{bmatrix} \\ &= \begin{bmatrix}\cos\alpha_p\sin\gamma + \sin\alpha_p\sin\varphi\cos\gamma \\ -\cos\varphi\cos\gamma \\ \sin\alpha_p\sin\gamma - \cos\alpha_p\sin\varphi\cos\gamma\end{bmatrix}G_p\end{aligned}$$

To obtain the static moment error, the force error in the body frame is multiplied by the respective moment arm x_m and z_m.

$$\begin{aligned}\vec{M}_0^b &= \begin{bmatrix}0 & 0 & y_m \\ 0 & 0 & -x_m \\ -y_m & x_m & 0\end{bmatrix}\vec{F}_0^b \\ &= \begin{bmatrix}y_m(\sin\alpha_p\sin\gamma - \cos\alpha_p\sin\varphi\cos\gamma) \\ x_m(\cos\alpha_p\sin\varphi\cos\gamma - \sin\alpha_p\sin\gamma) \\ -x_m\cos\varphi\cos\gamma - y_m(\cos\alpha_p\sin\gamma + \sin\alpha_p\sin\varphi\cos\gamma)\end{bmatrix}G_p\end{aligned}$$

Thus, neglecting the superscript b for body frame, the static mass error can be modeled as below:

$$\begin{bmatrix}\vec{F}_0 \\ \vec{M}_0\end{bmatrix} = \begin{bmatrix}\cos\alpha_p\sin\gamma + \sin\alpha_p\sin\varphi\cos\gamma \\ -\cos\varphi\cos\gamma \\ \sin\alpha_p\sin\gamma - \cos\alpha_p\sin\varphi\cos\gamma \\ y_m(\sin\alpha_p\sin\gamma - \cos\alpha_p\sin\varphi\cos\gamma) \\ x_m(\cos\alpha_p\sin\varphi\cos\gamma - \sin\alpha_p\sin\gamma) \\ -x_m\cos\varphi\cos\gamma - y_m(\cos\alpha_p\sin\gamma + \sin\alpha_p\sin\varphi\cos\gamma)\end{bmatrix}G_p$$

Appendix B: NACA Proprotor Geometry

Appendix C: NACA Proprotor Test Data

The freestream and proprotor tip speed ratio λ_∞ were regulated during the test according to Table 2.

Appendix D: Description of Computation Procedure

In this appendix, the proportor model were summarized in a suggested way of implementation.

Table C1. NACA proprotor test data

	$\lambda_\infty = 0.06$				$\lambda_\infty = 0.14$			
α_p (°)	C_T	C_Q	C_N	C_n	C_T	C_Q	C_N	C_n
0	0.0233	0.0076	0.0000	0.0000	0.0186	0.0059	0.0000	0.0000
15	0.0234	0.0077	0.0072	0.0005	0.0187	0.0060	0.0016	0.0009
30	0.0236	0.0078	0.0015	0.0010	0.0204	0.0066	0.0033	0.0019
45	0.0239	0.0079	0.0022	0.0015	0.0222	0.0073	0.0052	0.0028
60	0.0244	0.0081	0.0028	0.0019	0.0244	0.0080	0.0063	0.0036
75	0.0250	0.0082	0.0033	0.0021	0.0274	0.0089	0.0068	0.0040
90	0.0257	0.0083	0.0035	0.0023	0.0315	0.0101	0.0067	0.0041

Table C2. NACA proprotor test data (continued).

	$\lambda_\infty = 0.22$				$\lambda_\infty = 0.32$			
α_p (°)	C_T	C_Q	C_N	C_n	C_T	C_Q	C_N	C_n
0	0.0139	0.0051	0.0000	0.0000	0.0052	0.0037	0.0000	0.0000
15	0.0147	0.0054	0.0013	0.0011	0.0073	0.0042	0.0025	0.0018
30	0.0167	0.0060	0.0038	0.0025	0.0117	0.0053	0.0052	0.0037
45	0.0198	0.0071	0.0064	0.0039	0.0168	0.0069	0.0087	0.0058
60	0.0244	0.0086	0.0080	0.0048	0.0236	0.0091	0.0118	0.0076
75	0.0293	0.0100	0.0096	0.0056	0.0309	0.0112	0.0141	0.0089
90	0.0364	0.0120	0.0090	0.0058	0.0386	0.0136	0.0129	0.0093

The model takes the following parameters as inputs: (1) proprotor geometry: R, $\beta(r)$, $c(r)$ (or estimations of integrals I_1, I_2, I_3 in Eqs. (29)–(31)); (2) proprotor axial performance: thrust coefficient $C_T(0, \lambda_\infty)$ and power coefficient $C_P(0, \lambda_\infty)$; (3) freestream operating conditions: tip-speed ratio λ_∞ and rotor incidence angle α_p.

Inflow ratios were needed to normalize freestream including :

$$\text{Climb inflow ratio - } \lambda_c = \lambda_\infty \cos\alpha_p$$
$$\text{Rotor advance ratio - } \mu = \lambda_\infty \sin\alpha_p$$

Proprotor linear approximation includes the interpolation from axial performance data of zero thrust/power tip-speed ratios : $\lambda_{\infty_{0T}}$, $\lambda_{\infty_{0P}}$; and axial thrust and power coefficients : $C_T(0, \lambda_c)$ and $C_P(0, \lambda_c)$.

The high incidence correction factor $\delta(\mu, \lambda_c)$ is calculated from

$$\delta(\mu, \lambda_c) = \frac{3}{2}\cos\beta' \left[1 + \frac{\sigma'}{\tan\beta'}\left(1 + \sqrt{1 + \frac{2\tan\beta'}{\sigma'}}\right) \times \left(1 - \frac{\lambda_c}{\sqrt{\lambda_c^2 + \mu^2}}\right)\right].$$

The thrust and power ratio η_T, η_P at incidence angle could be computed as

$$\eta_T = 1 + \frac{(\mu/\bar{r}')^2}{2(1 - \lambda_c/\lambda_{\infty_{0T}})}$$
$$\eta_P = 1 + \frac{(\mu/\bar{r}')^2}{2(1 - \lambda_c/\lambda_{\infty_{0P}})}$$

Thrust and power coefficients at incidence are resolved by multiplying the equivalent zero-incidence coefficients with η_T, η_P such that

$$C_T(\mu, \lambda_c) = C_T(0, \lambda_c)\,\eta_T$$
$$C_P(\mu, \lambda_c) = C_P(0, \lambda_c)\,\eta_P$$

Induced inflow ratio λ_i is calculated from the resultant thrust coefficient through momentum theory.

Model coefficients for off-axis efforts are computed for

Dynamic pressure coefficient,

$$f(\lambda_i) = \frac{\pi^{\frac{3}{2}}\lambda_\infty^{\frac{1}{2}}(\lambda_\infty + \lambda_i)\left[\lambda_\infty(\lambda_\infty + \lambda_i) + (\lambda_\infty + 2\lambda_i)^2\right]}{\lambda_\infty^2 + (\lambda_\infty + 2\lambda_i)^2}$$

Geometric coefficients,

$$\Delta = \frac{(\sigma I_2 - 2\lambda_i)(\sigma I_2 + 4\lambda_i)}{\sigma(1 + \sigma I_2)} \text{ and } m = \frac{\sigma I_2 + 4\lambda_i}{2(1 + \sigma I_3)}$$

Normal force and in-plane moment gradient around zero incidence angle are found from

$$\left.\frac{\partial C_N}{\partial \alpha_p}\right|_{\alpha_p = 0} = \frac{1}{2\pi^2}\frac{k_s f(\lambda_i)\sigma I_1}{\frac{I_1}{I_1 - \Delta} + k_a \sigma I_1}$$
$$\left.\frac{\partial C_n}{\partial \alpha_p}\right|_{\alpha_p = 0} = \frac{1}{\pi^2}\frac{k_s f(\lambda_i) m}{1 + k_a \sigma(I_1 - \Delta)}$$

Finally, normal force and in-plane moment at high incidence are resolved:

$$C_N = \frac{2\lambda_{\infty_{0P}} - \lambda_\infty \cos\alpha_p}{2\lambda_{\infty_{0P}} - \lambda_\infty}\sin\alpha_p \left.\frac{\partial C_N}{\partial \alpha_p}\right|_{\alpha_p = 0, \lambda_\infty}$$
$$C_n = \frac{2\lambda_{\infty_{0T}} - \lambda_\infty \cos\alpha_p}{2\lambda_{\infty_{0T}} - \lambda_\infty}\sin\alpha_p \left.\frac{\partial C_N}{\partial \alpha_p}\right|_{\alpha_p = 0, \lambda_\infty}$$

References

[1]EVTOL Aircraft Directory, available at http://evtol.news/aircraft, accessed December 3, 2019, Electric VTOL News by the Vertical Flight Society.

[2]Harris, R. G., "Forces on Propeller due to Sideslip," Technical Report 427, British Aeronautical Research Council, London, UK, 1918.

[3]Glauert, H., "The Stability Derivatives of an Airscrew," Technical Report No. 642, British Aeronautical Research Council, London, UK, 1919.

[4]Ribner, H. S., "Propellers in Yaw," TR 820, NACA, Washington, DC, 1945.

[5]Ribner, H. S., "Formulas for Propellers in Yaw and Charts of the Side-Force Derivative," TR 819, NACA, Washington, DC, 1945.

[6]De Young, J., "Propeller at High Incidence," *Journal of Aircraft*, Vol. 2, (3), 1964, pp. 241–250, DOI: 10.2514/3.43646.

[7]Leishman, J. G., *Principles of Helicopter Aerodynamics*, Cambridge University Press, New York, NY, 2000, Chapter 3.

[8]Peters, D. A., and HaQuang, N., "Dynamic Inflow for Practical Applications," *Journal of American Helicopter Society*, Vol. 33, (4), 1988, pp. 64–68.

[9]Leng, Y., Yoo, H., Jardin, T., Bronz, M., and Moschetta, J.-M., "Aerodynamic Modelling of Propeller Forces and Moments at High Angle of Incidence," AIAA 2019-1332, Proceedings of the AIAA Applied Aerodynamics Conference and AIAA SciTech 2019 Forum, San Diego, CA, January 7–11, 2019.

[10]Theys, B., Dimitriadis, G., Hendrick, P., and De Schutter, J., "Experimental and Numerical Study of Micro-Aerial-Vehicle Propeller Performance in Oblique Flow," *Journal of Aircraft*, Vol. 54, (3), 2017, pp. 1076–1084. DOI: 10.2514/1.C033618.

[11]Gill, R., and D'Andrea, R., "Computationally Efficient Force and Moment Models for Propellers in UAV Forward Flight Applications," *Drones*, Vol. 3, (4), 2019, 77. DOI: 10.3390/drones3040077.

[12]Johnson, W., *Helicopter Theory*, Princeton University Press, Princeton, NJ, 1980, pp. 126–133.

[13]Bramwell, A.R.S., "Some Remarks on the Induced Velocity Field of a Lifting Rotor and on Glauert's Formula," Technical Report No. 1301, British Aeronautical Research Council, London, UK, 1974.

[14]Phillips, W. F., *Mechanics of Flight*, John Wiley & Sons, Hoboken, NJ, 2004, p. 131.

[15]Von Mises, R., *Theory of Flight*, Dover Publications, New York, NY, 1959, pp. 302–309.

[16]Leng, Y., Jardin, T., Bronz, M., and Moschetta, J.-M., "Experimental Analysis of Propeller Forces and Moments at High Angle of Incidence," AIAA 2019-1331, Proceedings of the AIAA Applied Aerodynamics Conference and AIAA SciTech 2019 Forum, San Diego, CA, January 7–11, 2019.

[17]Gessow, A., and Myers, G. C., *Aerodynamics of the Helicopter*, MacMillan, New York, NY, 1952, Ch. 8.

[18]Rumph, L. B., "Propeller Forces due to Yaw and Their Effect on Airplane Stability," *Journal of the Aeronautical Sciences*, Vol. 9, (12), 1942, pp. 465–470.

[19]Goates, J. T., "Development of an Improved Low-Order Model for Propeller-Wing Interactions," Master's thesis, Utah State University All Graduate Theses and Dissertations, 7394, 2018.

[20]Harris, F. D., "Rotor Performance at High Advance Ratio: Theory Versus Test," NASA, CR 2008–215370, 2008.

[21]Johnson, W., "NASA Design and Analysis of Rotorcraft," NASA, TP 2015–218751, 2015.

[22]Jo, Y., Jardin, T., Gojon, R., Jacob, M. C., and Moschetta, J.-M., "Prediction of Noise From Low Reynolds Number Rotors with Different Number of Blades using a Non-Linear Vortex Lattice Method," Proceedings of the 25th AIAA/CEAS Aeroacoustics Conference, Delft, The Netherlands, May 20–23, 2019.

[23]Gourdain, N., Singh, Deepali., Jardin, T., and Prothin, S., "Analysis of the Turbulent Wake Generated by a Micro Air Vehicle Hovering Near the Ground with a Lattice Boltzmann Method," *Journal of the American Helicopter Society*, **62**, 042003 (2017), DOI: 10.4050/JAHS.62.042003.

[24]Theys, B., Dimitriadis, G., Andrianne, T., Hendrick, P., and De Schutter, J., "Wind Tunnel Testing of a VTOL MAV Propeller in Tilted Operating Mode," Proceedings of the 2014 International Conference on Unmanned Aircraft Systems Proceedings, Orlando, FL, May 27–30, 2014.

[25]Yaggy, P. F., and Rogallo, V. L., "A Wind-Tunnel Investigation of Three Propellers through an Angle-of-Attack Range from 0 Deg to 85 Deg," NASA, TN D-318, 1960.

[26]Hoerner, S. F., *Fluid-Dynamic Drag: Practical Information on Aerodynamic Drag and Hydrodynamic Resistance*, Hoerner Fluid Dynamics, Bakersfield, CA, 2001, Ch. IV.